1 # Characterization of Shallow Oceanic Precipitation using Profiling
2 # and Scanning Radar Observations at the Eastern North Atlantic ARM
3 # Observatory

4
5 Katia Lamer[1], Bernat Puigdomènech Treserras[2], Zeen Zhu[3], Bradley Isom[4], Nitin Bharadwaj[4], and
6 Pavlos Kollias[3,5]

7
8 [1.] Department of Earth and Atmospheric Science, The City College of New York
9 [2.] Department of Atmospheric and Oceanic Sciences, McGill University
10 [3.] School of Marine and Atmospheric Sciences, Stony Brook University
11 [4.] Atmospheric Measurement and Data Sciences, Pacific Northwest National Laboratory
12 [5.] Department of Environmental and Climate Sciences, Brookhaven National Laboratory

13
14 Correspondance: Katia Lamer, klamer@ccny.cuny.edu

15
16 ## Abstract

17
18 Shallow oceanic precipitation variability is documented using 2nd generation radars located
19 at the Atmospheric Radiation Measurement (ARM) Eastern North Atlantic observatory: the Ka-
20 band ARM zenith radar (KAZR2), the Ka-band scanning ARM cloud radar (KaSACR2) and the
21 X-band scanning ARM precipitation radar (XSAPR2). First, the radars and measurement post-
22 processing techniques, including sea clutter removal and calibration against collocated
23 disdrometer and Global Precipitation Mission (GPM) observations are described. Then, we present
24 how a combination of profiling radar and lidar observations can be used to estimate adaptive (in
25 both time and height) parameters that relate radar reflectivity (Z) to precipitation rate (R) in the
26 form $Z = \alpha R^\beta$ which we use to estimate precipitation rate over the domain observed by XSAPR2.
27 Furthermore, Constant Altitude Plan Position Indicator (CAPPI) gridded XSAPR2 precipitation
28 rate maps are also constructed.

29
30 Hourly precipitation rate statistics estimated from the three radars differ; that is because KAZR2
31 is more sensitive to shallow virga and because XSAPR2 suffers from less attenuation that
32 KaSACR2 and as such is best suited to characterize intermittent and mesoscale-organized
33 precipitation. Further analysis reveals that precipitation rate statistics obtained by averaging 12h
34 of KAZR2 observations can be used to approximate that of a domain of 2,500 km^2 averaged over
35 similar time periods. However, it was determined that KAZR2 is unsuitable to characterize domain
36 average precipitation rate over shorter periods. But even more fundamentally, these results suggest
37 that observations cannot produce objective domain precipitation estimate and that forward-
38 simulators should be used to guide high temporal-resolution model evaluation studies.
39
40
41
42
43
44
45

46   **1.0 Introduction**

47

48   Characterizing shallow oceanic precipitation is all-important to improving our
49   understanding of shallow cloud systems since precipitation is related to a number of cloud process
50   all of which may affect cloud properties. For example, precipitation leads to a reduction in the
51   droplet number via the collision-coalescence process and of the liquid water path through
52   sedimentation. Furthermore, a number of modeling studies have suggested that drizzle
53   organization, intensity and subcloud layer evaporation could play a role in organizing
54   stratocumulus cloud decks on the mesoscale (Zhou et al., 2017; Savic-Jovcic and Stevens, 2008;
55   Wang and Feingold, 2009; Yamaguchi and Feingold, 2015; Zhou et al., 2018). Ultimately, these
56   controls may alter low cloud radiative properties and climate (Wood, 2012). Quantification, over
57   a domain of several kilometers, of marine drizzle cell precipitation rate, along with sub cloud layer
58   evaporation rate, thermodynamic properties and dynamics could provide additional observational
59   constrains for modeling studies unfortunately, such observations remain challenging to collect
60   over the ocean.

61

62   Although satellite-based microwave sensors can infer the spatial distribution of liquid water path
63   (Wood and Hartmann, 2006; Miller and Yuter, 2013) and precipitation rate (Ellis et al., 2009;
64   Adler et al., 2009; Rapp et al., 2013) they have poor horizontal resolution and suffer from surface
65   inference causing them to under sample the cloud field variability and to underreport boundary-
66   layer cloud and precipitation occurrence (Schumacher and Houze Jr, 2000; Rapp et al., 2013). In
67   contrast, airborne (Stevens et al., 2005; Wood et al., 2011; Moyer and Young, 1994; Vali et al.,
68   1998; Paluch and Lenschow, 1991; Sharon et al., 2006) and ship-based (Yuter et al., 2000;
69   Comstock et al., 2005; Feingold et al., 2010) sensors can resolve the spatial/temporal variability
70   of the cloud and precipitation field, but field campaigns deploying such sensors are often expensive
71   to conduct and limited in temporal duration (Stevens et al., 2003; Bretherton et al., 2004; Rauber
72   et al., 2007). Island-based observatories such as the U.S. Department of Energy (DOE)
73   Atmospheric Radiation Measurement (ARM) Eastern North Atlantic observatory (ENA, Mather
74   et al., 2016; Kollias et al., 2016) and the Barbados Cloud Observatory (BCO, Lamer et al., 2015;
75   Stevens et al., 2016) operating profiling and scanning remote sensors can provide long-term
76   statistics of marine light precipitation.

77

78   Beyond detecting, quantifying precipitation rate from warm clouds is especially challenging since
79   the droplets they contain do not generate the typical polarimetric signals required of common
80   precipitation rate retrievals (e.g., Villarini and Krajewski, 2010; Gorgucci et al., 2000). As an
81   alternative to polarimetric signatures, a combination of sensors is typically required to retrieve
82   precipitation rate (R); Combinations of radar reflectivity (Z) and in-situ measurements have led to
83   the development of Z-R relationships (Wood, 2005; Comstock et al., 2004; VanZanten et al., 2005;
84   Vali et al., 1998) however, these tend not to be universally applicable since they are based on
85   assumptions about the drizzle particle size distribution which may vary with factors such as aerosol
86   loading and liquid water path. Moreover, relying on surface disdrometer measurements to
87   characterize warm precipitation may be especially unsuitable at the ENA where i) a large fraction
88   of the precipitation does not reach the surface (Yang et al., 2018), ii) precipitation reaching the
89   ground typically does so with an intensity below the detection limit of most optical-based
90   disdrometers ($\sim 10^{-2}$ mm hr^{-1}) and iii) evaporation is an active process such that water drop size
91   distribution information retrieved at one height may not be appropriate to represent the entire

Atmospheric
Measurement
Techniques
Discussions

92   atmospheric column. Alternatively, a method combining radar reflectivity and lidar backscatter
93   measurements has been proposed to retrieve R without assumptions about the drizzle particle size
94   distribution (Intrieri et al., 1993; O'Connor et al., 2005); Because of the rarity of scanning lidar
95   observations, this technique has only been used to retrieved R in the column and cannot be used to
96   address the concerns present in recent studies suggesting that scanning systems are essential to
97   map domain properties (Oue et al., 2016).
98
99   Here we propose to exploit the availability of collocated vertically-pointing radar and lidar as well
100   as scanning radar systems to characterize marine precipitation rate variability over a domain of 40-
101   60 km around the ENA observatory. The ENA, with its abundance of marine boundary layer
102   precipitating clouds, is an ideal location for such study (Rémillard and Tselioudis, 2015; Wood,
103   2012).Observations from the Ka-band ARM Zenith Radar (KAZR2) and zenith-pointing
104   ceilometer lidar are combined to estimate adaptive (both in time and height) *Z-R* relationships
105   which we then use to estimate precipitation rate across the domain observed by the X-band
106   Scanning ARM Precipitation Radar (XSAPR2). Domain-average and time-average precipitation
107   rate estimates obtained from zenith-pointing and scanning observations are compared to document
108   the complementarity and applicability of each sensor in documenting precipitation rate from warm
109   boundary layer clouds.
110
111   **2.0 Eastern North Atlantic Observatory**
112
113   In October 2013, the ARM program established a permanent observatory in the Eastern North
114   Atlantic on the island of Graciosa (~60 km^2 area; 39.1°N, 28.0°W). The site, located within the
115   Azores archipelago, straddles the boundary between the subtropics and the midlatitudes and as
116   such is subject to a wide range of different meteorological conditions including periods of
117   relatively undisturbed trade-wind flow, midlatitude cyclonic systems and associated fronts, and
118   periods of extensive low-level cloudiness (Rémillard and Tselioudis, 2015). The observatory hosts
119   an extensive instrument suite including three second generation radar systems: the Ka-band ARM
120   Zenith Radar (KAZR2), the dual-frequency Ka-and W-band Scanning ARM Cloud Radar
121   (SACR2) and the X-band Scanning ARM Precipitation Radar (XSAPR2) which's specifications
122   are listed in Table 1. A short description of the radar systems is provided here with emphasis on
123   changes in configuration from the first to the second generation.
124
125   **2.1 KAZR2**
126
127   KAZR2 operates at 34.8 GHz (λ = 8.6 mm) and is an upgraded version of the KAZR that
128   replaced the ARM MilliMeter Cloud Radar (MMCR, Kollias et al., 2016). KAZR2 uses an
129   Extended Interaction Klystron (EIK) amplifier with a 2.2 kW peak power and 5 % duty cycle. Its
130   dual receiver configuration allows the simultaneous transmission of a long (4 µs) pulse with
131   frequency modulation (pulse compression) for higher sensitivity (~-44 dBZ at 1 km not
132   considering signal integration gain) at ranges from 737 m from the radar to 18 km and a short pulse
133   (200 ns) with a sensitivity of (~-32.5 dBZ at 1 km not considering signal integration gain) at ranges
134   from 72 m to 18 km. KAZR2 has a narrow (0.3°) 3-dB antenna bandwidth and is nominally
135   operated with a range resolution of 30 m, a temporal resolution of 2 sec and is set to record the full
136   radar Doppler spectrum with 256 or 512 FFT points. KAZR2 transmits a horizontal pulse and
137   receives both horizontal and vertical polarization such that the only polarimetric information it can

Atmospheric
Measurement
Techniques
Discussions

138   measure is linear depolarization ratio.
139
140   **2.2 KaSACR2**
141
142   KaSACR2 is a fully polarimetric radar that operates at 35.3 GHz (λ = 8.5 mm) and is an
143   upgraded version of the single polarization KaSACR described in Kollias et al., (2014a,b). The
144   KaSACR2 also uses an EIK amplifier with a 2.2 kW peak power, has a 5 % duty cycle and a 3-dB
145   antenna beamwidth of 0.3°. Currently, it is operated with a short pulse, although it could be
146   operated with a longer pulse with pulse compression for increased sensitivity. Owing to its narrow
147   beam width KaSACR2 must scan rather slowly (3-6° s^{-1}) to collect observation with a sensitivity
148   of ~-15 dBZ at 20 km (not considering signal integration gain). The KaSACR2 conducts a cloud
149   sampling strategy that includes different modes (Kollias et al., 2014a,b). Here, because of our
150   interest to map precipitation structure and rate over a large horizontal domain, we only use
151   observations collected in Plan Position Indicator (PPI) configuration at 0.5° elevation angle over
152   a 160° wide azimuth sector. The KaSACR2 conducts a PPI scan every 15 min and takes 2 min to
153   collect each PPI. The KaSACR2 employs frequency hopping and staggered pulse repetition time
154   techniques to mitigate artifacts due to second trip echoes and velocity aliasing; This however
155   comes at the expense of preventing the collection of the full Doppler spectrum.
156
157   **2.3 XSAPR2**
158
159   XSAPR2 operates at 9.5 GHz (λ = 3.2 cm); It is an upgraded version of the XSAPR as it
160   operates with an improved digital receiver and a larger antenna (5 m) which results to an
161   exceptionally narrow 3-dB antenna beamwidth of 0.45°. The requirement for the XSAPR2 to have
162   a narrow antenna beamwidth emerged from a need to reduce the impact of sea-clutter at low-
163   elevations and maintain high angular resolution over a 60 km radius in order to resolve small scale
164   oceanic precipitating clouds. XSAPR2 uses a high-power Magnetron with a 300kW peak power
165   and a maximum duty cycle of 0.1 %. Under nominal operational conditions, the XSAPR2 transmits
166   a 60 m long pulse and scans at a relatively slow rate (6° s^{-1}) to collect observations with a sensitivity
167   of ~-21 dBZ at 20km (not considering integration gain). The XSAPR2 volume coverage pattern
168   (VCP) scan strategy consists of a series of PPI scans every 0.5° elevation between the angles of 0°
169   and 5°. Because of considerable beam blockage in the southerly direction a 160° azimuth sector
170   coverage is achieved. The VCP scan (i.e. the entire set of PPI scans) is completed within 5 min
171   and subsequently repeated. Horizontal and vertical polarization are possible for both transmit and
172   receive states, meaning XSAPR2 collects a full suite of polarimetric variables while in scanning
173   mode.
174
175   **3.0 Radar Observations Post-Processing**
176
177   Radar observations require considerable post-processing for the removal of non-
178   meteorological targets before they can be scientifically interpreted or used to retrieve geophysical
179   quantities such as precipitation rate. Radar data post-processing is described in section 3.1 and
180   cross-comparison between different systems for calibration is described in section 3.2. Note that
181   the KAZR2 data used for analysis are from "enakazrgeC1.a1" files, KaSACR2 data are from
182   "enakasacrppivhC1.a1" files and the XSAPR2 from the "enaxsaprsecD1.00 files". All data files
183   were obtained from the ARM archive (https://www.archive.arm.gov/discovery/).

Atmospheric
Measurement
Techniques
Discussions

3.1 Removal of Non-Meteorological Targets

First, signal processing artifacts (e.g. second trip echoes) and echoes of non-meteorological origin (e.g., biological echoes, sea-clutter, and ground-clutter) are identified and removed.

The KaSACR2 system operates in fully polarimetric mode and uses staggered pulse repetition time and frequency hopping to automatically remove second trip echoes, perform velocity dealiasing and increase the number of independent samples (Pazmany et al., 2013). The XSAPR2 systems operates using a magnetron system which is coherent on receive (i.e., transmitted pulse phase is random). For the XSAPR2, the removal of second trip echoes is done using Normalized Coherent Power (NCP) which is the coherency of the received pulse with respect to the last transmitted pulse. For atmospheric echoes within maximum unambiguous range, NCP is high since the radar receiver is phase-locked to the phased of the last transmitted pulse. Outside of the maximum unambiguous range, NCP is low since the radar receiver has already phase-locked on the phase of another transmitted pulse. Here, an NCP threshold of 0.3 is used to identify echoes originating from outside the maximum unambiguous range (i.e. second trip echoes).

Biological targets such as insect and birds often contaminate radar observations especially over land (e.g., Luke et al., 2008). Their occurrence varies with atmospheric condition, time of the year, and time of the day (Alku et al., 2015). KAZR2 observations at the ENA seem minimally impacted by biological echoes. Furthermore, the fact that the bulk of the KaSACR2 and XSAPR2 observations are collected over open ocean and that Graciosa is a small island suggests that biological targets should not be a concern at this particular location.

On the other hand, low elevation angle observations are susceptible to sea-clutter contamination. Research on radar sea-clutter characterization and remediation has been ongoing for over 20 years (e.g., Horst et al., 1978; Gregers-Hansen and Mital, 2009; Nathanson et al., 1991); Observational and modeling studies suggest that factors such as oceanic wave properties (related to local wind speed and direction), swell and air density streams can affect sea-clutter occurrence. Radar characteristics such as wavelength, wave polarization, beam width and grazing angle are also known to affect sea-clutter characteristics, amounts and our ability to isolate atmospheric returns from sea-clutter. Here, observations collected over a range of wind conditions during nearly 100 hours of clear sky conditions are used to examine how sea-clutter characteristics vary with radar wavelength, beam width and beam elevation angle.

First, the distribution of sea-clutter reflectivities as measured by the XSAPR2 and KaSACR2 at elevation 0.5° are compared to document the antenna beam width effect (Fig. 1d). The KaSACR2 (0.3° 3-dB antenna beam width) sea-clutter reflectivity distribution is narrower with a peak at -21 dBZ and a majority of echoes below -15 dBZ (Fig. 1d black line) while the XSAPR2 (0.45° 3-dB antenna beam width) sea-clutter reflectivity distribution is wider, peaks at -18 dBZ and covers a range from -40 dBZ to +10 dBZ (Fig. 1d red line). This can be explained by the XSAPR2 wider antenna beam width which results in a larger fraction of the radiated energy to hit ocean waves, causing higher ocean clutter return power. Similar to beam width, elevation angle affects how much sea is in the radar field of view and the spatial extent of observed sea-clutter. Figure 1d, shows that, at 1.0° elevation, XSAPR2 sea-clutter reflectivity peaks at a lower reflectivity of -25 dBZ (blue line) and Fig. 1b$_3$ shows that in this configuration it frequently (> 25 % of the time)

Atmospheric
Measurement
Techniques
Open Access
Discussions

230 detects clutter only over a domain of 10 km radius around the site which is much less than it detects
231 when collecting observations at 0.5° elevation (significant clutter in a 20 km radius around the
232 site Fig. 1a$_3$).
233
234 Now that we have characterized sea-clutter intensity and frequency of occurrence using clear sky
235 observations we next evaluate its impact on the detection of meteorological targets using
236 observations containing mixture of hydrometeor and sea-clutter. To isolate hydrometeors from
237 clutter, we exploit the correlation coefficient ρ_{HV} which we know is affected by the relative
238 occurrence of signal to clutter; ρ_{HV} is typically close to 1 for liquid-phase hydrometeors and lower
239 for non-meteorological targets. Looking at KaSACR2 reflectivity and ρ_{HV} confirms that at Ka-
240 band wavelength the signal to clutter ratio is high and hydrometeors contributions dominate both
241 radar reflectivity and correlation coefficient measurements (Fig. 1c$_1$ and 1c$_2$, respectively). The
242 enhanced KaSACR2 signal-to-clutter ratio is attributed to two effects: i) its narrow beamwidth
243 which causes a smaller fraction of the transmitter energy to hit the sea surface and ii) its shorter
244 wavelength which creates a larger distinction between hydrometeor scattering - which follow
245 Rayleigh scattering $\sim 1/\lambda^4$ - and sea-clutter scattering – which follow $\sim 1/\lambda$ -.Using KaSACR2
246 observations has a guide to locate cloud and precipitation location (Fig 1c$_1$), it is apparent that it
247 is not possible to distinguish atmospheric signals from sea-clutter in XSAPR2 radar reflectivity
248 observation collected at 0.5° (Fig 1a$_1$).
249
250 Several techniques that use both time-domain and frequency domain filtering methods have been
251 proposed to discriminate between sea-clutter and meteorological targets in precipitation radar
252 observations (e.g., Torres and Zrnic, 1999; Siggia and Passarelli, 2004; Nguyen et al., 2008; Alku
253 et al., 2015). Ryzhkov et al. (2002) present an echo classification technique based on fuzzy logic
254 and a multiparameter dataset including radar reflectivity, mean Doppler velocity, spectrum width,
255 differential reflectivity, differential phase, linear depolarization ratio, and cross-correlation (ρ_{HV}).
256 In the current study, given the radars narrow beam width and short wavelength, an approach solely
257 based on ρ_{HV} is used to filter sea-clutter. Since cross-correlation between horizontal and vertical
258 cross-polar received powers is largest for spherical hydrometeors, we label observations with
259 ρ_{HV} larger than a certain threshold as atmospheric returns and the rest as sea-clutter. The analysis
260 of a large sample of ρ_{HV} observations during clear and cloudy sky conditions indicates that the use
261 of a threshold of 0.9 for KaSACR2 and an average (over 5 range gates and 5 azimuthal
262 measurements) threshold of 0.55 for the XSAPR2 can be used to isolate hydrometeor-dominated
263 from clutter-dominates observations. The proposed ρ_{HV} technique successfully isolates
264 atmospheric returns at the same location for both the X-band at 1.0° elevation and the reference
265 Ka-band 0.5° elevation (Fig. 1b$_2$ and c$_2$ respectively; pink regions). However, it only identifies a
266 fraction of the atmospheric returns in the X-band 0.5° elevation observations. There, additional
267 filtering, beyond the scope of this study, would be required to suppress the remaining sea-clutter
268 and recover the missing atmospheric returns (see (Moisseev and Chandrasekar, 2009; Unal, 2009)
269 who propose advanced technique). Given this, XSAPR2 cross validation and precipitation rate
270 maps will be estimated using observations collected at 1.0° elevation since it offers the best
271 compromise between proximity to the surface and minimum sea-clutter contamination.
272
273 **3.2 Radar Calibration**
274
275   Calibrated reflectivity observations are necessary to perform quantitative precipitation rate

Atmospheric
Measurement
Techniques
Discussions

276　retrievals. Following Kollias et al. (2019), KAZR2 calibration is performed using collocated
277　surface-based Parsivel laser disdrometer equivalent radar reflectivity estimates during light
278　precipitation events as well as CloudSat observations collected over a small radius around the site.
279　We estimate that, during the period of interest (01/10/2018 to 04/01/2018), KAZR2 radar
280　reflectivity measurements are off by about +3-dB which we proceeded to correct for. The detailed
281　time-series of KAZR2 calibration offset is presented in Fig. 2a.

283　Comparison of total (Fig. 3a) and range resolved (Fig. 3b) histograms of radar reflectivity
284　measured by KAZR2 (pre-calibration) and KaSACR2 at zenith confirm that during the analysis
285　period the KaSACR2 matched KAZR2. For this reason, KaSACR2 radar reflectivity
286　measurements were also adjusted by the calibration constant depicted in Fig. 2a. Note how this
287　comparison between the KAZR2 and KaSACR2 was performed between 1.5 to 5 km to avoid any
288　differences in the reported radar reflectivities due to differences in how they detect ground/sea-
289　clutter.

291　Calibrating the XSAPR2 radar reflectivity measurements is more challenging since it does not
292　perform profiling observations and as such it cannot be benchmarked against disdrometer and
293　KAZR2 observations. Here, we assess the calibration of the XSAPR2 radar using observations
294　from the Global Precipitation Measurement (GPM) Ku-band frequency of the Dual-frequency
295　Precipitation Radar (DPR) when the satellite track crosses within a 245 km radius of the XSAPR2
296　radar site. For comparison, ground-based XSAPR2 reflectivity measurements are smoothed and
297　interpolated to the satellite sampling volume: The azimuth-range measurements are smoothed
298　using the 0.71° 3-dB beamwidth antenna weighting function of the GPM DPR (5-km footprint).
299　Nearest neighbor is then used to match the satellite measurements in the horizontal plane while
300　linear interpolation is used to match them in the vertical plane (Warren et al., 2018). Matched
301　XSAP2 radar reflectivity measurements are compared to GPM DPR corrected reflectivity
302　measurements (GPM product version V06A (Iguchi et al., 2010)). Considering differences in radar
303　sensitivity, radar reflectivity measurements with returns smaller than 14 dBZ are not considered
304　during the calibration procedure (Toyoshima et al., 2015) and only periods when both radars
305　coincidently detect significant precipitation are used to perform calibration. For the analysis
306　period, a total of 3 GPM overpasses with significant precipitation were observed for a total number
307　of 1516 data points for the comparison.

309　An example of concurrent XSAPR2 and GPM DPR radar reflectivity observations are shown in
310　Fig. 4a and c respectively. The example shows that both radars detected several shallow
311　precipitation cells with cloud top heights between 3 and 4 km (Fig. 3b). Beyond agreeing in their
312　location, both radars (XSAPR2 and GPM DPR) are found to agree on the reflectivity intensity of
313　these precipitation echoes. To confirm their agreement, we estimated Contour of Frequency by
314　Altitude Diagram (CFAD) of the differences in radar reflectivities between the matched XSAPR2
315　and GPM DPR for all 1516 available observations (Fig. 4b). This comparison shows no noticeable
316　difference (i.e., no bias) between 1.5 and 3.5 km. Though in the lowest kilometer GPM's DPR
317　tends to overestimate the near surface radar reflectivity (Fig. 4b), a scatter plot between the
318　matched GPM DPR and XSAPR2 radar reflectivities confirms the overall lack of significant bias
319　between the two radars (Fig. 4d). This leads us to conclude that, for the observation period between
320　01/10/2018 to 04/01/2018, the XSAPR2 was well calibrated and does not require any radar
321　reflectivity adjustments.

Atmospheric
Measurement
Techniques
Open Access
Discussions

EGU

4.0 Radar Reflectivity-Based Precipitation Rate Retrievals

Distinct considerations must be taken to quantitatively retrieve precipitation rate from KAZR2, XSAPR2 and KaSACR2 measurements.

4.1 KAZR2

Intrieri et al. (1993) and later O'Connor et al. (2005) proposed a technique to constrain water drop size distribution using lidar backscatter (related to water drop cross-section) and radar Doppler spectral width (related to the width of the water drop size distribution). This radar-lidar technique can be used to estimate precipitation rate at all levels in the subcloud layer when collocated radar and ceilometer observations are available. We apply this technique to the vertically pointing ceilometer lidar and KAZR2 pair operating at the ENA. The O'Connor et al. (2005) technique requires ceilometer backscatter to be calibrated and remapped to the radar spatio-temporal resolution (here 2 s x 30 m). Ceilometer backscatter is calibrated following a variation of the O'Connor et al. (2004) technique by scaling observed path-integrated backscatter in thick stratocumulus to match theoretical cloud lidar ratio values. Satisfactory conditions for ceilometer backscatter calibration are identified as the first (in time) 20-min periods each day with standard deviation of lidar ratio smaller than 1.5. The observed backscatter during the "satisfactory 20-min period" are input to Hogan (2006)'s multi scattered model to determine a daily backscatter calibration factor. For days where satisfactory conditions are not observed, a climatological calibration factor of 1.35 is used to calibrate the observed backscatter. For the current analysis period, the ceilometer backscatter calibration constant was estimated to vary around 1.35+/- 0.08. (Fig 2b). Calibrated ceilometer backscatter is subsequently mapped on the KAZR2 time-height grid using a nearest neighbor approach.

This radar-lidar technique generates time-height maps of precipitation rate from 200 m above ground level to 90 m below cloud base height which are filtered for aerosol contamination. We use the clear-sky – according to KAZR - calibrated lidar backscatter signals as a reference for aerosol behavior, lidar calibrated backscatter values below the mean clear-sky calibrated backscatter value at each height, depicted as the black vertical line in Fig. 2c, are systematically removed from the analysis to leave only drizzle signals. In additional to aerosol contaminated returns, unphysical values with median diameter smaller than 10 μ m or equal or large to 1000 μ m are also removed from our analysis.

Two one-hour examples of cloud location (black dots) and precipitation rate estimated using this technique are shown in Fig. 5a and b. Because of evaporation, the most intense precipitation rates are observed near cloud base height and a significant fraction of the precipitation does not reach the surface and falls as virga.

4.2 XSAPR2

As previously mentioned, the estimation of the precipitation rate for the XSAPR2 i) cannot depend on the use of polarimetric observations, because of the absence of polarimetric signature from spherical drizzle drops and ii) cannot depend on the use of disdrometer-based estimates of the relationship between the radar reflectivity (Z) and the precipitation rate (R), because

Atmospheric
Measurement
Techniques
Open Access
Discussions

EGU

368 observations collected at the surface may not be representative of other levels in the subcloud layer
369 especially at the ENA where evaporation is an active process.
370
371 To accommodate changes in drizzle drop size distribution with height which could be associate
372 for example to changes in aerosol loading or evaporation, we propose to construct adaptive (both
373 with time and height) Z-R relationships in the form $Z = \alpha R^{\beta}$ from precipitation rates retrieved
374 through the KAZR-ceilometer technique (see section 4.1). Every 30 min, independently for every
375 level in the subcloud layer, retrieved zenith precipitation rates (R in mm hr^{-1}) and calibrated KAZR
376 reflectivity (Z in mm^6 m^{-3}) reported during a 12-h window around that time are related through the
377 relationship:
378
379 $$\log_{10}(Z) = log_{10}(\alpha) + \beta \cdot log_{10}(R) \qquad\qquad (1)$$
380
381 The prefactor α and exponent β are estimated using a total least square regression technique only
382 considering R between $10^{-3.5}$ and $10^{0.5}$ mm hr^{-1} and only if at least 350 precipitation detections are
383 available. When too few observations are available, average (for the period of the current study)
384 α and β are used. A 12h time window was determined to be the best compromise between data
385 density and least change in water drop size distribution characteristics.
386
387 To evaluate the adaptive Z-R, we apply three different precipitation retrieval techniques to
388 KAZR2 reflectivity observations: We compare precipitation rate statistics retrieved following
389 the O'Connor et al. (2005) technique (ideal technique, red), to those estimated using Z-R
390 relationships constructed using fixed (approach proposed by Comstock et al. (2004), green) or
391 adaptive (approach proposed here, black) coefficients (presented in Fig. 6e and f respective).
392 Figure 6f shows that the proposed adaptive Z-R relationships can reproduce the precipitation
393 rate statistics obtained using the ideal O'Connor et al. (2005) technique. The same cannot be
394 said from using traditional fixed Z-R relationships such as that proposed by Comstock et al.
395 (2004) which tends to create an underestimation of precipitation intensity (Fig. 6e).
396
397 Fig. 6a and b respectively present time series of α and β near cloud base (i.e., 90 m below
398 cloud base height) for a 30-day long period that overlaps with the second phase of the ACE-
399 ENA field campaign: Again for comparison we illustrate our adaptive coefficients (black), the
400 Comstock et al. (2004) constant coefficients (dashed green) and coefficients estimated from
401 surface-based Parsivel laser disdrometer measurements (dashed orange). The gradual increase
402 in both the adaptive α and β coefficients over time is consistent with reports of observed
403 conditions indicating a transition from shallow precipitation at the end of January to deep
404 frontal precipitation at the end of February. CFADs of α and β (Fig. 6c and d respectively)
405 show how the adaptive α additionally has a tendency to increase with distance from cloud base
406 (from top to bottom), which is consistent with the evaporation of small drops that leads to an
407 increase in mean drop size and has been previously reported by Comstock et al. (2004) and
408 discussed in VanZanten et al. (2005).
409
410 Figure 5c and d show how, by applying the adaptive Z-R, XSAPR2 reflectivity observations
411 collected at 1° elevation can be converted to precipitation rate. Note how the adaptive Z-R
412 relationships can be directly applied to clutter-filtered calibrated XSAPR2 radar reflectivity
413 measurements since two-way gas attenuation at X-band is negligible (generally amounts to 0.03

Atmospheric
Measurement
Techniques
Discussions

414   dB km^{-1} according to Rosenkranz (1998)).
415
416   **4.3 KaSACR2**
417
418   Before quantitatively estimating precipitation rate from KaSACR radar reflectivity
419   measurements, we also consider how its wavelength responds to the presence of atmospheric
420   gases. Rosenkranz (1998) propagation model suggests that, for the conditions observed at the
421   ENA, two-way gas attenuation of Ka-band signals can amount to 0.25 dB km^{-1}. Although this may
422   seem small and can be insignificant when collecting observations of boundary layer clouds in
423   profiling mode, in scan mode, attenuation of Ka-band reflectivity by atmospheric gas can amount
424   to 10 dB at 40 km range (Fig. 9 difference between the black and green curve) and as such
425   should not be neglected. Also note that in addition to the gaseous attenuation, Ka-band radars
426   suffer from considerable liquid water attenuation. According to Matrosov (2005), the
427   relationship between one way liquid attenuation a (dB km^{-1}) and precipitation rate R (mm hr^{-1})
428   ^{1}) is very robust ($a = 0.28R$). His findings were verified using Mie scattering calculations on
429   all particle size distributions observed by the ENA Parsivel laser disdrometer. Fig. 7e
430   illustrates an example of observations collected by the KaSACR at 0.5 elevation on
431   02/13/2018, in this example, liquid contributed anywhere from 2 to 10 dB in total attenuation
432   at Ka-band over the 40 km observation domain. If left uncorrected, liquid attenuation can lead
433   to errors in preciptiation rate estimates up to 3 mm hr^{-1} in this example (Fig. 6f). Fig. 6 also
434   shows reflectivity and precipitation rate for the XSAPR2 which, as discussed in th previous
435   section, only suffer from negligible attenuation (Fig 6g and h). Comparing observations from
436   the unattenuated XSAPR2 (Fig. 6h) and observations from the KaSACR2 corrected for both
437   gas and liquid attenuation (Fig. 6d) also highlights the fact that even after all correction are
438   performed the KaSACR2 "realized" sensitivity does not allow it to detect some of the
439   precipitation the more sensitive XSAPR2 can detect. The range-dependent sensitivity of both
440   sensors can be contrasted in Fig. 9c.
441
442   **5.0 Complementary of different radar systems in Characterizing Light Precipitation**
443   **Variability**
444
445   As discussed in section 2.0, the KAZR2, KaSACR2 and XSAPR2 radars sample light
446   precipitation using very different transmission and sampling strategies. In this section we highlight
447   some of the advantages and tradeoffs of using each radar system to characterize different aspects
448   of light precipitation variability.
449
450   For illustration purposes, we compare, over the course of 36 hours between 00:00 UTC February
451   2 and 12:00 UTC February 3, hourly precipitation rate variability in the forms of frequency of
452   occurrence in different precipitation rate bins (pdf). Figure 8a shows estimates from the scanning
453   XSAPR2 collecting observation in PPI mode covering a domain between 2.5 and 40 km at 1°
454   elevation thus transecting heights between ~100 m and 750 m (also refer to Fig. 9a to visualize the
455   XSAPR2 sampling geometry). Figure 8b and c respectively show estimates from the vertically
456   pointing KAZR2 200 m above the surface and 90 m below cloud base which was around 850 m.
457
458   From Fig. 8b and c, it is evident that KAZR2, with its high sensitivity, is especially well suited to
459   document light precipitation and drizzle falling at a rate as low as 10^{-4} mm hr^{-1}. KAZR2

460 observations show a reduction in the number of precipitation events and in precipitation intensity
461 from cloud base (Fig. 8c) towards the surface (Fig. 8b). This supports previous hypothesis that at
462 the ENA a large fraction of the light precipitation falls in the form of virga (Ahlgrimm and Forbes,
463 2014; Yang et al., 2018). Under these circumstances, where the character of precipitation changes
464 dramatically with height and its intensity is very low (below 10^{-3} mmhr^{-1}), scanning radar
465 observation at a fixed elevation may become inadequate to characterize surface precipitation over
466 a large domain owing to Earth curvature effects. Fig. 9a illustrates the height above the surface of
467 a 1° elevation scan with distance away from the radar; at a distance of 10-20 km the radar beam is
468 already 250 m above the surface while at a distance of 20-30 km this same radar beam is now 500
469 m from the surface. This non-uniformity of the radar beam height with distance makes scanning
470 cloud radar observations at one elevation angle more adequate to document the character of
471 vertically uniform precipitation. The rapid sampling rate of the KAZR2 also allows it to describe
472 the vertical structure of precipitation variability at a high temporal (scales as short as 2s).

474 On the other hand, one drawback of vertically pointing KAZR2 observations is that they are limited
475 to sampling only those precipitation events advected overhead. It is not uncommon to temporally
476 average vertically pointing observation to create a proxy for domain average statistics, however as
477 depicted in Fig. 5 it may be difficult to address the domain representativeness of one-hour of
478 vertically pointing precipitation rate estimates. It can also be challenging to interpret the mesoscale
479 organization of the precipitation field using vertically pointing observations alone; Scanning
480 systems such as the XSAPR2 can help fill this gap. Figure 5c and d show XSAPR2 1° elevation
481 PPI scans collected at 10:00 am and 8:00 am respectively which corresponds to the center time of
482 the KAZR2 time-height observations presented in Fig. 5a and b. XSAPR2 can observe the
483 structure and scales of popcorn precipitation and squall line precipitation over a domain of roughly
484 2,500 km². In its current configuration, the XSAPR2 system can be used to document the
485 horizontal structure and temporal variability of light-to-moderate precipitation on scales of ~5
486 minutes. Referring back to Fig. 8a hourly precipitation rate pdfs, it is evident that by covering a
487 larger domain XSAPR2 is able to observe a larger number of near surface sporadic precipitation
488 events such as that observed on Feb 03 around 0:00 and of isolated deep convective events
489 responsible for more intense precipitation ($R > 3$ mm hr^{-1}) such as that observed on Feb 03 around
490 8:00.

492 Now constrasting the two scanning radar XSAPR2 and KaSACR2. Although the Ka-band
493 SACR experiences less sea-clutter than the X-band SAPR, because of needs for cloud
494 sampling, it only currently performs one PPI scan at 0.5° every 15 min which limits its
495 temporal resolution. In addition, based on their technical specifications (Table 1), the XSAPR2
496 single pulse radar sensitivity is approximately 10 dB higher than that of the KaSACR2 (Fig. 9c
497 blue and black line respectively) and that is before considering that the Ka-band SACR also suffer
498 from significantly more attenuation from atmospheric gases (Fig. 9c green line) and liquid water
499 which even if corrected for still decrease it's "realized" sensitivity. For all these reasons, we
500 conclude that the XSAPR2 is more suitable for characterizing light precipitation variability
501 over large domains.

503 **6.0 Gridded Domain Precipitation Rate Estimation**

505 One way for scanning radars to overcome some of the limitation of their scanning strategy

Atmospheric
Measurement
Techniques
Open Access
EGU
Discussions

506   is to develop horizontal, two-dimensional, gridded maps of the radar observables and other
507   quantities (i.e. precipitation rate) using measurements collected at different elevations angles (i.e.,
508   construct constant altitude plan position indicator (CAPPI) maps). Here, gridded XSAPR2
509   CAPPI's are constructed as follows: We perform the polar to Cartesian transformation for each
510   individual reflectivity measurement using a standard atmosphere radio propagation model which
511   considers the height of the beam above the Earth surface, and the distance between the radar and
512   the projection of the beam along the Earth surface (Doviak and Zrnic, 1993). Using these Cartesian
513   coordinates each PPI is mapped on a 100 m horizontal grid for which each grid point is populated
514   using a triangulation technique (i.e., the nearest three observations are linearly interpolated to
515   populate the grid cell). Then, every 100 m in the horizontal, a grid point at constant altitude is
516   populated by i) a measured value if falling on an elevation where observations were collected or
517   otherwise ii) a weighted average of the gridded data from the three closest PPI; The weight being
518   the inverse horizontal distance from the grid location. The aforementioned adaptive *Z-R*
519   relationships are then applied to the Cartesian grid reflectivity observations to produce
520   precipitation rate CAPPI such as the one illustrated in Fig. 9b. Figure 9 shows a Cartesian
521   coordinate constant altitude plan position indicator (CAPPI) map of precipitation rate constructed
522   around an altitude of 500 m using XSAPR2 observations collected between 1 and 5° elevation
523   (Fig. 9a, red color). This figure also illustrates how scanning radar sensitivity is range dependent
524   such that weak precipitation rates can only be detected close to the sensor (Fig. 9b light grey
525   colors). Producing an unbiased assessment requires the application of a uniform sensitivity
526   threshold over the entire domain observed by the scanning radar which creates a tradeoff between
527   documenting a large domain and documenting weak precipitation events. As quantified in Fig. 9c
528   at a distance of 40 km the XSAPR2 is only capable of detecting precipitation events of intensity
529   larger than $10^{-2.8}$ mm hr^{-1} and any desire to document weaker precipitation rate events would
530   further limit domain size.

7.0 Domain Average Precipitation Rate - When do Temporal and Horizontal Precipitation Variability Converge?

535   The addition of the XSAPR2 at the ENA observatory offers new insights into precipitation
536   variability and organization over a domain of 40-60 km radius around the size. However, the
537   XSAPR2 data record is not as long as the KAZR data record which now spans 5 years at the ENA
538   even totaling up to 7.5 years if we consider the Cloud, Aerosols, and Precipitation in the Marine
539   Boundary Layer (CAP-MBL) campaign that took place at the site from April 2009 until January
540   2011 (Wood et al., 2005). Because of their longer data record, profiling radar observations have
541   the potential to inform us about decadal precipitation variability both temporal and structural.
542   However, with vertically pointing observations, it is near impossible to disentangle temporal
543   evolution from horizontal structure. Classical approaches rely on Taylor hypothesis of frozen
544   turbulence to convert elapsed time to horizontal dimension using the horizontal wind speed
545   responsible for advecting cloud and precipitation overhead. While widely used, little research has
546   been conducted to determine the validity and limitations of this assumption (see Oue et al. (2016)
547   for a discussion on cloud fraction). In this section we seek to determine how long does one need
548   to observe precipitation advected overhead to gather statistical precipitation information
549   equivalent to that of an 80 km wide domain.

551   Precipitation rate reported by XSAPR2 over a domain of 40 km radius around the site at 1°

Atmospheric
Measurement
Techniques
Discussions

Open Access

EGU

552 elevation are used to evaluate the representativeness of KAZR2 observations collected 200 m
553 above the surface. To remove any bias caused by variations in minimum performance of both
554 sensors, a minimum precipitation rate threshold of $10^{-2.8}$ mm hr^{-1} is applied to both sensors
555 reflecting the detectability of the XSAPR2 over the selected domain. Statistics for both sensors are
556 estimated using different set averaging time intervals (30 min, 1 h, 3 h, 12 h and 24 h) which allows
557 us to monitor the temporal variability of domain-average precipitation rate. For XSAPR2, using a
558 sliding window, we average all 5-min PPI observations collected during the chosen time interval.
559 For KAZR, we center the time window on the XSAPR2 estimates and average all 2-s observations
560 collected during the chosen time interval.

562 Focusing on features such as the width, the minimum, maximum and modes of the precipitation
563 rate statistical distribution; Results indicate that neither 30 min nor 1h averaging of KAZR
564 precipitation rate estimates can be used to replicate the precipitation rate statistics corresponding
565 to those of domain averaged over 30 min (Fig. 10 left column). Figure 10's 3rd and 4th columns/3rd
566 and 4th rows, suggests that longer time averages (3h and 12 h) of KAZR2 observations capture the
567 most frequently occurring precipitation mode of domain-average precipitation rate on 3h and 12 h
568 timescales. Convergence between XSAPR2 and KAZR2 time-average precipitation rate estimates
569 is best (in terms of root mean square error (RMSE)) when considering the variability of domain-
570 average precipitation rate over timescales of 12 h (RMSE 13.4%); 12-h average domain-average
571 precipitation rate pdf from XSAPR2 and 12-h average precipitation rate pdf from KAZR are
572 similar in both magnitude and mode location.

574 Although these results are estimated with few observational cases (30 days), they clearly suggest
575 that XSAPR2 observations are necessary to characterize short-term (< 3 h) domain-average
576 precipitation rate characteristics. They also suggest that longer-term (12 h) domain-average
577 precipitation rate characteristics can be estimated by averaging either XSAPR2 or KAZR2
578 observations using time-windows of similar lengths.

580 **8.0 Summary and Conclusions**

582   The ARM ENA observatory is the first island-based climate research facility equipped with
583 collocated radars and lidars capable of sampling light oceanic precipitation. Here we presented the
584 characteristics and first light observations from three state-of-the-art 2nd generation radar systems:
585 the Ka-band Zenith radar (KAZR2), the Ka-band scanning ARM cloud radar (KaSACR2) and the
586 X-band scanning ARM precipitation radar (XSAPR2),

588 One of the initial concerns of operating scanning cloud and precipitation radars over the ocean is
589 the impact of sea-clutter, especially at low-elevation angles. Nearly one hundred hours of clear sky
590 observations were used to characterize the properties of sea-clutter in KaSACR2 and XSAPR2
591 observations. Analysis of clear and cloudy skies periods and intercomparison of the meteorological
592 and non-meteorological echoes of the KaSACR2 made it possible to design a relatively simple
593 filtering technique to isolate precipitation echoes in XSAPR2 observations. In short, a threshold
594 on normalized coherent power (< 0.3) and on average (5x5 window) cross-correlation (< 0.55),
595 can mitigate second-trip echoes and sea-clutter echoes. Everything considered, we find that
596 XSAPR2 observations collected at 1° elevation, albeit suffering from more clutter contamination
597 than KaSACR2, offer the best compromise between clutter contamination and proximity to the

598   surface.
599
600   Measurement calibration is also essential to quantitative precipitation rate retrieval. We applied
601   Kollias et al. (2019) technique to calibrate KAZR2 radar reflectivity measurements using Parsivel
602   disdrometer and CloudSat observations. Because they were found to match, the same offset is
603   applied to the KaSACR2 observations. To calibrate the XSAPR2 reflectivity measurements we
604   relied on a statistical comparison with GPM Ku-band radar observations collected around the ENA
605   site. The analysis indicated no noticeable offset; thus, no calibration offset was applied to the
606   XSAPR2. These techniques could be used in the future as a supplement to the ARM radar
607   engineering group efforts to characterize the ENA radars reflectivity measurements.
608
609   We capitalized on the availability of closely collected (in both time and physical distance) KAZR2,
610   ceilometer lidar and XSAPR2 measurement to estimate precipitation rate. Precipitation rates
611   retrieved using the O'Connor et al. (2005) radar-lidar technique have the advantage of being
612   estimated without assumptions on the drizzle drop size distribution shape and can accommodate
613   changes in aerosol loading, liquid water path and evaporation. Unfortunately, for a lack of scanning
614   lidar observations, we cannot apply this technique to scanning radar observations. Instead, we
615   showed how relating the retrieved precipitation rates in the column to radar reflectivity can be used
616   to estimate adaptive (in both time and height) parameters that related observed radar reflectivity
617   (Z) to precipitation rate (R) in the form $Z = \alpha R^\beta$ which can be applied to retrieve precipitation
618   rate of the domain covered by scanning cloud radars. We report these adaptive parameters for the
619   period between 01/10/2018 and 04/01/2018 which includes the second phase of the ACE-ENA
620   campaign. These adaptive parameters were showed to capture changes in drop size distribution
621   with height as well as temporal changes in the cloud field.
622
623   Throughout this work, comparing precipitation rate statistics estimated by all three sensors
624   highlighted the following:
625
626   1) Because of strong signal attenuation by gases and liquid at Ka-band, X-band radars are
627   more suited for precipitation mapping especially over large domains.
628   2) When the character of precipitation varies rapidly with height for instance owing to an
629   active evaporation process, zenith-pointing radars are more suited for precipitation
630   characterization;
631   3) However, zenith-pointing observations collected over periods shorter than 12h should not
632   be considered representative of a domain especially one as large as 2,500 km^2 (i.e., ~40 km
633   radius half circle).
634   4) Estimates of domain precipitation rate variability on timescale of 12 hours can be captured
635   by averaging 12h of zenith-pointing radar observations collected at 200 m above the
636   surface.
637   5) Shorter term domain precipitation rate variability can only be capture by scanning
638   precipitation radars.
639   6) Scanning sensors are also better suited to document sporadic and horizontal homogeneous
640   precipitation including precipitation presenting mesoscale organization.
641
642   In a nutshell, the considerable differences in precipitation rate statistics estimated by the XSAPR2
643   and KAZR2 challenge our ability to objectively estimate precipitation rate statistics over a domain

14

Atmospheric
Measurement
Techniques
Discussions

644   for applications such as evaluation of high-resolution model output. Factors such as instrument
645   sensitivity, sampling temporal resolution, sampling height and domain size should always be
646   considered when comparing model output to observations for example through the use of forward
647   simulators.
648
649   **Authors contributions**
650
651   K. Lamer coordinated the project, performed the intercomparisons between the precipitation rates
652   produced by the three radars and produced the final manuscript draft. P. Kollias supervised Z. Zhu
653   and B. Puigdomènech Treserras as they respectively analyzed the KAZR2 and both the KaSACR2
654   and XSAPR2 observations; Analysis steps included performing data post-processing, calibration
655   and precipitation rate retrievals. B. Puigdomènech Treserras also produced the CAPPI part of this
656   work. B. Isom and N. Bharadwaj provided a wealth of information about the radar system
657   characteristics as well as guidance on radar data calibration. All coauthors have read the
658   manuscript draft and have contributed comments.
659
660   **Acknowledgments**
661

670

671   **Data availability**
672
673   All ARM data streams are available online at: http://www.archive.arm.gov/discovery/. All
674   GPM data streams are available online at https://pmm.nasa.gov/data-access/downloads/gpm.
675
676
677
678
679
680
681
682
683
684
685
686
687
688
689

Atmospheric
Measurement
Techniques

Discussions

References

692 Adler, R. F., Wang, J.-J., Gu, G., and Huffman, G. J.: A ten-year tropical rainfall climatology based
693   on a composite of TRMM products, Journal of the Meteorological Society of Japan. Ser.
694   II, 87, 281-293, 2009.

695 Ahlgrimm, M., and Forbes, R.: Improving the representation of low clouds and drizzle in the
696   ECMWF model based on ARM observations from the Azores, Monthly Weather Review,
697   142, 668-685, 2014.

698 Alku, L., Moisseev, D., Aittomäki, T., and Chandrasekar, V.: Identification and suppression of
699   nonmeteorological echoes using spectral polarimetric processing, IEEE Transactions on
700   Geoscience and Remote Sensing, 53, 3628-3638, 2015.

701 Bretherton, C. S., Uttal, T., Fairall, C. W., Yuter, S. E., Weller, R. A., Baumgardner, D., Comstock,
702   K., Wood, R., and Raga, G. B.: The EPIC 2001 stratocumulus study, Bulletin of the
703   American Meteorological Society, 85, 967-978, 2004.

704 Comstock, K. K., Wood, R., Yuter, S. E., and Bretherton, C. S.: Reflectivity and rain rate in and
705   below drizzling stratocumulus, Quarterly Journal of the Royal Meteorological Society,
706   130, 2891-2918, 2004.

707 Comstock, K. K., Bretherton, C. S., and Yuter, S. E.: Mesoscale variability and drizzle in southeast
708   Pacific stratocumulus, Journal of the Atmospheric Sciences, 62, 3792-3807, 2005.

709 Doviak, R., and Zrnic, D.: Doppler Radar and, 1993.

710 Ellis, T. D., L'Ecuyer, T., Haynes, J. M., and Stephens, G. L.: How often does it rain over the
711   global oceans? The perspective from CloudSat, Geophysical Research Letters, 36, 2009.

712 Feingold, G., Koren, I., Wang, H., Xue, H., and Brewer, W. A.: Precipitation-generated
713   oscillations in open cellular cloud fields, Nature, 466, 849, 2010.

714 Gorgucci, E., Scarchilli, G., and Chandrasekar, V.: Sensitivity of multiparameter radar rainfall
715   algorithms, Journal of Geophysical Research: Atmospheres, 105, 2215-2223, 2000.

716 Gregers-Hansen, V., and Mital, R.: An empirical sea clutter model for low grazing angles, Radar
717   Conference, 2009 IEEE, 2009, 1-5.

718 Hogan, R. J.: Fast approximate calculation of multiply scattered lidar returns, Applied Optics, 45,
719   5984-5992, 2006.

720 Horst, M., Dyer, F., and Tuley, M.: Radar sea clutter model, Antennas and Propagation, 1978, 6-
721   10.

722 Iguchi, T., Seto, S., Meneghini, R., Yoshida, N., Awaka, J., and Kubota, T.: GPM/DPR level-2
723   algorithm theoretical basis document, NASA Goddard Space Flight Center, Greenbelt,
724   MD, USA, Tech. Rep, 2010.

725   Intrieri, J. M., Stephens, G. L., Eberhard, W. L., and Uttal, T.: A method for determining cirrus
726   cloud particle sizes using lidar and radar backscatter technique, Journal of Applied
727   Meteorology, 32, 1074-1082, 1993.

728   Kollias, P., Bharadwaj, N., Widener, K., Jo, I., and Johnson, K.: Scanning ARM cloud radars. Part
729   I: Operational sampling strategies, Journal of Atmospheric and Oceanic Technology, 31,
730   569-582, 2014a.

731   Kollias, P., Jo, I., Borque, P., Tatarevic, A., Lamer, K., Bharadwaj, N., Widener, K., Johnson, K.,
732   and Clothiaux, E. E.: Scanning ARM cloud radars. Part II: Data quality control and
733   processing, Journal of Atmospheric Oceanic Technology, 31, 583-598, 2014b.

734   Kollias, P., Clothiaux, E. E., Ackerman, T. P., Albrecht, B. A., Widener, K. B., Moran, K. P.,
735   Luke, E. P., Johnson, K. L., Bharadwaj, N., and Mead, J. B.: Development and applications
736   of ARM millimeter-wavelength cloud radars, Meteorological Monographs, 57, 17.11-
737   17.19, 2016.

738   Kollias, P., Puigdomènech Treserras, B., and Protat, A.: Calibration of the 2007-2017 record of
739   ARM Cloud Radar Observations using CloudSat, Atmos. Meas. Tech. Discuss., 2019, 1-
740   30, 10.5194/amt-2019-34, 2019.

741   Lamer, K., Kollias, P., and Nuijens, L.: Observations of the variability of shallow trade wind
742   cumulus cloudiness and mass flux, Journal of Geophysical Research: Atmospheres, 120,
743   6161-6178, 2015.

744   Luke, E. P., Kollias, P., Johnson, K. L., and Clothiaux, E. E.: A technique for the automatic
745   detection of insect clutter in cloud radar returns, Journal of Atmospheric and Oceanic
746   Technology, 25, 1498-1513, 2008.

747   Mather, J., Turner, D., and Ackerman, T.: Scientific maturation of the ARM Program,
748   Meteorological Monographs, 57, 4.1-4.19, 2016.

749   Matrosov, S. Y.: Attenuation-based estimates of rainfall rates aloft with vertically pointing Ka-
750   band radars, Journal of Atmospheric and Oceanic Technology, 22, 43-54, 2005.

751   Miller, M., and Yuter, S.: Detection and characterization of heavy drizzle cells within subtropical
752   marine stratocumulus using AMSR-E 89-GHz passive microwave measurements,
753   Atmospheric Measurement Techniques, 6, 1-13, 2013.

754   Moisseev, D. N., and Chandrasekar, V.: Polarimetric spectral filter for adaptive clutter and noise
755   suppression, Journal of Atmospheric and Oceanic Technology, 26, 215-228, 2009.

756   Moyer, K. A., and Young, G. S.: Observations of mesoscale cellular convection from the marine
757   stratocumulus phase of "FIRE", Boundary-Layer Meteorology, 71, 109-133, 1994.

758   Nathanson, F. E., Reilly, J. P., and Cohen, M. N.: Radar design principles-Signal processing and
759   the Environment, NASA STI/Recon Technical Report A, 91, 1991.

Atmospheric
Measurement
Techniques
Discussions

760 Nguyen, C. M., Moisseev, D. N., and Chandrasekar, V.: A parametric time domain method for
761   spectral moment estimation and clutter mitigation for weather radars, Journal of
762   Atmospheric and Oceanic Technology, 25, 83-92, 2008.

763 O'Connor, E. J., Illingworth, A. J., and Hogan, R. J.: A technique for autocalibration of cloud lidar,
764   Journal of Atmospheric and Oceanic Technology, 21, 777-786, 2004.

765 O'Connor, E. J., Hogan, R. J., and Illingworth, A. J.: Retrieving stratocumulus drizzle parameters
766   using Doppler radar and lidar, Journal of Applied Meteorology, 44, 14-27, 2005.

767 Oue, M., Kollias, P., North, K. W., Tatarevic, A., Endo, S., Vogelmann, A. M., and Gustafson, W.
768   I.: Estimation of cloud fraction profile in shallow convection using a scanning cloud radar,
769   Geophysical Research Letters, 43, 2016.

770 Paluch, I., and Lenschow, D.: Stratiform cloud formation in the marine boundary layer, Journal of
771   the atmospheric sciences, 48, 2141-2158, 1991.

772 Pazmany, A. L., Mead, J. B., Bluestein, H. B., Snyder, J. C., and Houser, J. B.: A mobile rapid-
773   scanning X-band polarimetric (RaXPol) Doppler radar system, Journal of Atmospheric and
774   Oceanic Technology, 30, 1398-1413, 2013.

775 Rapp, A. D., Lebsock, M., and L'Ecuyer, T.: Low cloud precipitation climatology in the
776   southeastern Pacific marine stratocumulus region using CloudSat, Environmental Research
777   Letters, 8, 014027, 2013.

778 Rauber, R. M., Stevens, B., Ochs III, H. T., Knight, C., Albrecht, B. A., Blyth, A., Fairall, C.,
779   Jensen, J., Lasher-Trapp, S., and Mayol-Bracero, O.: Rain in shallow cumulus over the
780   ocean: The RICO campaign, Bulletin of the American Meteorological Society, 88, 1912-
781   1928, 2007.

782 Rémillard, J., and Tselioudis, G.: Cloud regime variability over the Azores and its application to
783   climate model evaluation, Journal of Climate, 28, 9707-9720, 2015.

784 Rosenkranz, P. W.: Water vapor microwave continuum absorption: A comparison of
785   measurements and models, Radio Science, 33, 919-928, 1998.

786 Ryzhkov, A., Zhang, P., Doviak, R., and Kessinger, C.: Discrimination between weather and sea
787   clutter using Doppler and dual-polarization weather radars, Proc. 27th General Assembly
788   of the International Union of Radio Science, 3, 2002.

789 Savic-Jovcic, V., and Stevens, B.: The structure and mesoscale organization of precipitating
790   stratocumulus, Journal of the Atmospheric Sciences, 65, 1587-1605, 2008.

791 Schumacher, C., and Houze Jr, R. A.: Comparison of radar data from the TRMM satellite and
792   Kwajalein oceanic validation site, Journal of Applied Meteorology, 39, 2151-2164, 2000.

793 Sharon, T. M., Albrecht, B. A., Jonsson, H. H., Minnis, P., Khaiyer, M. M., van Reken, T. M.,
794   Seinfeld, J., and Flagan, R.: Aerosol and cloud microphysical characteristics of rifts and

795   gradients in maritime stratocumulus clouds, Journal of the Atmospheric Sciences, 63, 983-
796   997, 2006.

797 Siggia, A., and Passarelli, R.: Gaussian model adaptive processing (GMAP) for improved ground
798   clutter cancellation and moment calculation, Proc. ERAD, 2004, 421-424.

799 Stevens, B., Lenschow, D. H., Vali, G., Gerber, H., Bandy, A., Blomquist, B., Brenguier, J.-L.,
800   Bretherton, C., Burnet, F., and Campos, T.: Dynamics and chemistry of marine
801   stratocumulus—DYCOMS-II, Bulletin of the American Meteorological Society, 84, 579-
802   594, 2003.

803 Stevens, B., Vali, G., Comstock, K. K., Wood, R., Van Zanten, M. C., Austin, P. H., Bretherton,
804   C. S., and Lenschow, D. H.: Pockets of open cells and drizzle in marine stratocumulus,
805   Bulletin of the American Meteorological Society, 86, 51-58, 2005.

806 Stevens, B., Farrell, D., Hirsch, L., Jansen, F., Nuijens, L., Serikov, I., Brügmann, B., Forde, M.,
807   Linne, H., and Lonitz, K.: The Barbados Cloud Observatory: Anchoring investigations of
808   clouds and circulation on the edge of the ITCZ, Bulletin of the American Meteorological
809   Society, 97, 787-801, 2016.

810 Torres, S. M., and Zrnic, D. S.: Ground clutter canceling with a regression filter, Journal of
811   Atmospheric and Oceanic Technology, 16, 1364-1372, 1999.

812 Toyoshima, K., Masunaga, H., and Furuzawa, F. A.: Early evaluation of Ku-and Ka-band
813   sensitivities for the global precipitation measurement (GPM) dual-frequency precipitation
814   radar (DPR), Sola, 11, 14-17, 2015.

815 Unal, C.: Spectral polarimetric radar clutter suppression to enhance atmospheric echoes, Journal
816   of atmospheric and oceanic technology, 26, 1781-1797, 2009.

817 Vali, G., Kelly, R. D., French, J., Haimov, S., Leon, D., McIntosh, R. E., and Pazmany, A.:
818   Finescale structure and microphysics of coastal stratus, Journal of the Atmospheric
819   Sciences, 55, 3540-3564, 1998.

820 VanZanten, M., Stevens, B., Vali, G., and Lenschow, D.: Observations of drizzle in nocturnal
821   marine stratocumulus, Journal of the Atmospheric Sciences, 62, 88-106, 2005.

822 Villarini, G., and Krajewski, W. F.: Review of the different sources of uncertainty in single
823   polarization radar-based estimates of rainfall, Surveys in Geophysics, 31, 107-129, 2010.

824 Wang, H., and Feingold, G.: Modeling mesoscale cellular structures and drizzle in marine
825   stratocumulus. Part I: Impact of drizzle on the formation and evolution of open cells,
826   Journal of the Atmospheric Sciences, 66, 3237-3256, 2009.

827 Warren, R. A., Protat, A., Siems, S. T., Ramsay, H. A., Louf, V., Manton, M. J., and Kane, T. A.:
828   Calibrating ground-based radars against TRMM and GPM, Journal of Atmospheric and
829   Oceanic Technology, 35, 323-346, 2018.

830   Wood, R.: Drizzle in stratiform boundary layer clouds. Part II: Microphysical aspects, Journal of
831   the Atmospheric Sciences, 62, 3034-3050, 2005.

832   Wood, R., and Hartmann, D. L.: Spatial variability of liquid water path in marine low cloud: The
833   importance of mesoscale cellular convection, Journal of Climate, 19, 1748-1764, 2006.

834   Wood, R., Bretherton, C., Leon, D., Clarke, A., Zuidema, P., Allen, G., and Coe, H.: An aircraft
835   case study of the spatial transition from closed to open mesoscale cellular convection over
836   the Southeast Pacific, Atmospheric Chemistry and Physics, 11, 2341, 2011.

837   Wood, R.: Stratocumulus clouds, Monthly Weather Review, 140, 2373-2423, 2012.

838   Yamaguchi, T., and Feingold, G.: On the relationship between open cellular convective cloud
839   patterns and the spatial distribution of precipitation, Atmospheric Chemistry and Physics,
840   15, 1237, 2015.

841   Yang, F., Luke, E. P., Kollias, P., Kostinski, A. B., and Vogelmann, A. M.: Scaling of drizzle virga
842   depth with cloud thickness for marine stratocumulus clouds, Geophysical Research Letters,
843   45, 3746-3753, 2018.

844   Yuter, S. E., Serra, Y. L., and Houze Jr, R. A.: The 1997 Pan American climate studies tropical
845   eastern Pacific process study. Part II: Stratocumulus region, Bulletin of the American
846   Meteorological Society, 81, 483-490, 2000.

847   Zhou, X., Heus, T., and Kollias, P.: Influences of drizzle on stratocumulus cloudiness and
848   organization, Journal of Geophysical Research: Atmospheres, 122, 6989-7003, 2017.

849   Zhou, X., Ackerman, A. S., Fridlind, A. M., and Kollias, P.: Simulation of Mesoscale Cellular
850   Convection in Marine Stratocumulus. Part I: Drizzling Conditions, Journal of the
851   Atmospheric Sciences, 75, 257-274, 2018.
852
853
854
855
856
857
858
859
860
861
862
863
864
865
866
867

Atmospheric
Measurement
Techniques
Discussions

868   **Tables**
869
870   Table 1 Specification of ARM ENA zenith and scanning second generation radars
871

	KAZR2		KaSACR2		XSAPR2	
Frequency (MHz)	34860		35290		9500	
Peak power (kW)	2.2		2.2		300	
Maximum Duty cycle (%)	5.0		5.0		0.1	
Pulse compression	Yes		Yes (but not on)		No	
Pulse length	4 µs	200 ns	?		0.66 µs	
Sensitivity single pulse (dBZ)	-32.5 (at 1 km)	-44 (at 1 km)	-15 (at 20 km)		-21 (at 20 km)	
Dead zone (m)	72	737	400		100	
Unambiguous range (km)	18		40		Over 100	
Gate spacing (m)	30		30		100	
Antenna size (m)	1.82		1.82		5.0	
3-dB Beam width (°)	0.3		0.3		0.45	
Scan rate (° s^{-1})	-		3		6	
Scan strategy	Zenith		PPI scan		VCP scan	
Elevation angle (°)	90		0.5		0 to 5 every 0.5	
Azimuthal sector (°)	-		360		160	
Scan time	3 s		2 min		5 min	
Scan Interval	Continuous		15 min			
Transmit polarization	H		Alternating H and V		Simultaneous H and V	
Received polarization	H and V		H and V		H and V	
Amplifier Type	Klystron (EIKA)		Klystron (EIKA)		Magnetron	
Signal processing	FFT		Pulse-pair	FFT	Pulse-pair	FFT
Doppler spectra	Yes		No	Yes	No	Yes
Second trip echo removal technique	Challenging		Frequency Hopping	Challenging	None	Coherent Power technique
Velocity dealiasing technique	Challenging		Staggered Pulse Repetition Time	Challenging	Challenging	

872
873
874
875

Atmospheric
Measurement
Techniques
Discussions
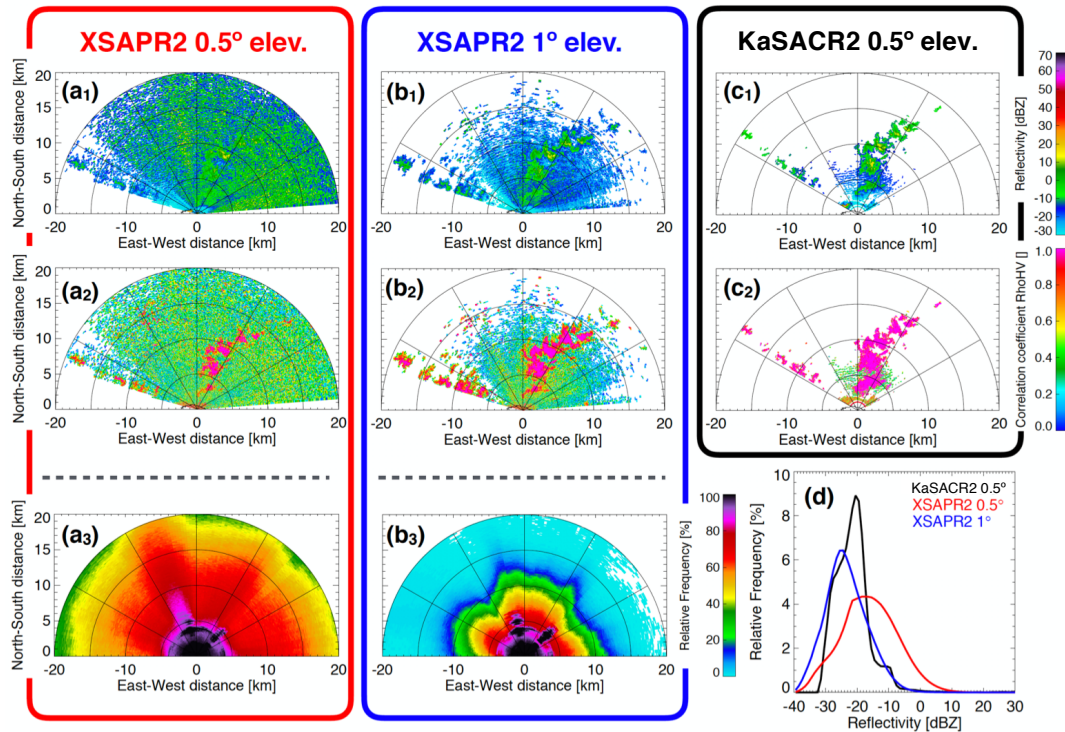
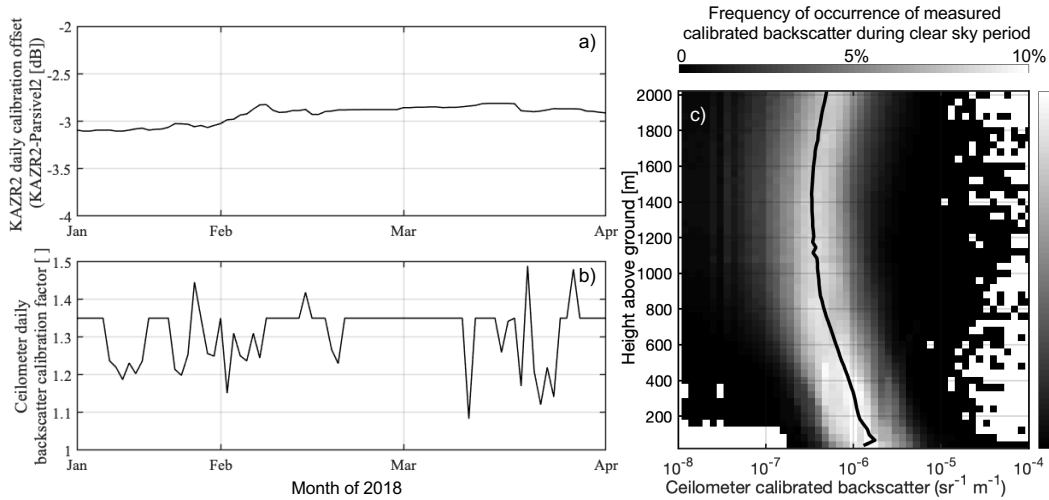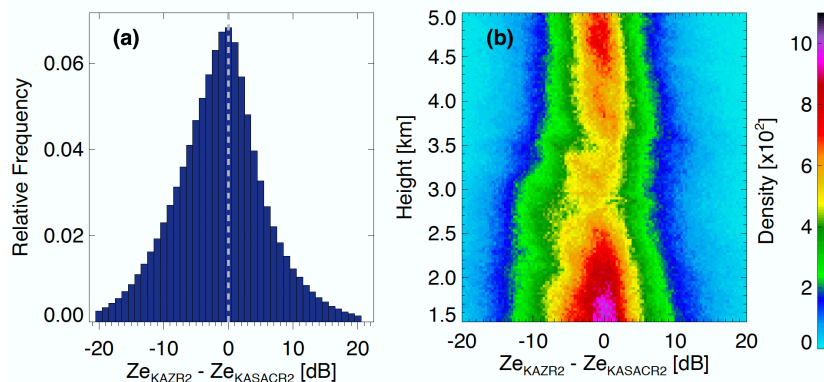# Figures

Figure 1. For significant echoes, 1) radar reflectivity, 2) correlation coefficient (ρ_{HV}) and 3) relative frequency of occurrence of clutter as observed by the a) XSAPR2 at 0.5° elevation, b) XSAPR2 at 1° elevation and c) KaSACR at 0.5° elevation. d) Clutter characteristics estimated using 93 hours of clear sky observations.

Atmospheric
Measurement
Techniques
Discussions

Open Access

886
887 **Figure 2.** a) Ka-band Zenith Radar (KAZR) calibration offset to be removed from the KAZR radar
888 reflectivity in order to match Parsivel Disdrometer radar reflectivity estimates. b) Ceilometer lidar
889 calibration factor to be multiplied to observed backscatter to match theoretical liquid cloud lidar
890 ratios. c) Frequency of occurrence of observed backscatter during clear sky conditions, solid black
891 line is interpreted as the mean aerosol backscatter signal, observations small than this threshold at
892 each height are eliminated from the drizzle analysis.
893
894

895
896 **Figure 3**. For period when KAZR2 and KaSACR2 are matched in time and range a) Difference in
897 radar reflectivity reported by both sensors over the ranges between 1.5 and 5.0 km, b) Difference
898 in radar reflectivity reported by both sensors as a function of range.
899

Atmospheric
Measurement
Techniques
Discussions
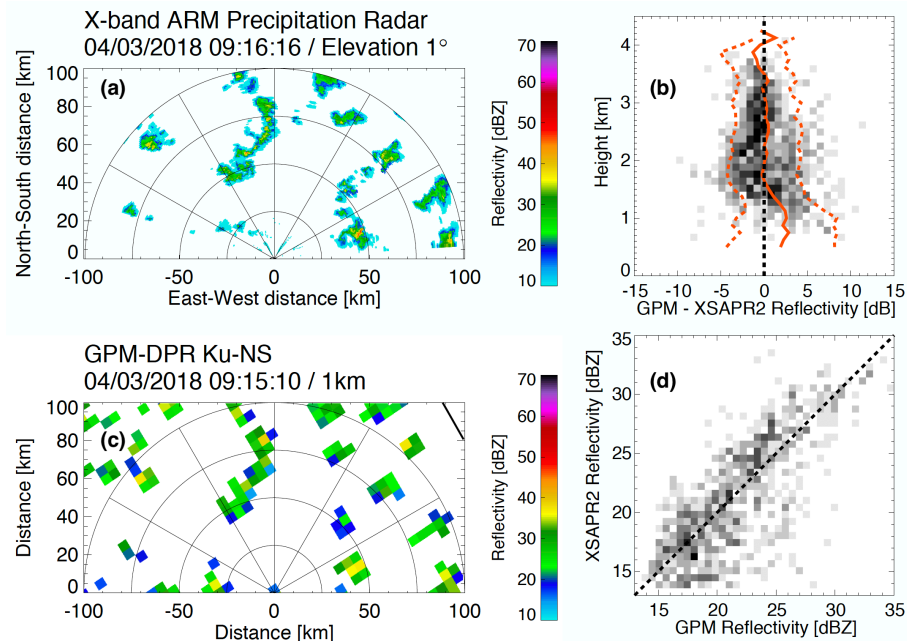
Figure 4. For the conditions that occurred on 04/03/2018 around 09:15 as observed by a) XSAPR2 radar reflectivity at 1° elevation and c) GPM-DPR Ku-band radar reflectivity at 1 km height. For the entire geometry-matching dataset with 1516 points used for the calibration b) Difference between the GPM-DPR Ku-band and XSAPR2 radar reflectivity measurements as a function of height and d) scatterplot comparing the XSAPR2 and GPM-DPR Ku-band reflectivities measurements.
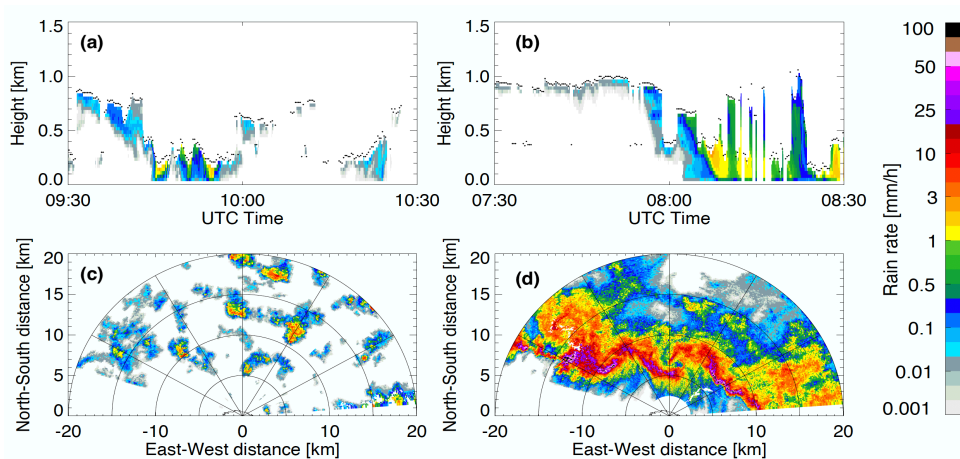
Figure 5. Retrieval of popcorn convection precipitation rate on 02/02/2018 using a) KAZR2 (zenith between 9:30 to 10:30 UTC) and c) KaSACR2 (1° elevation PPI at 10:00 UTC). Retrieval of squall line precipitation rate on 03/02/2018 using b) KAZR2 (zenith between 7:30 to 8:30 UTC) and d) KaSACR2 (1° elevation PPI at 8:00 UTC). Also indicated are the location of cloud bases (black dots in panels a-b). Note that KAZR2 is located at (0 km,0 km).
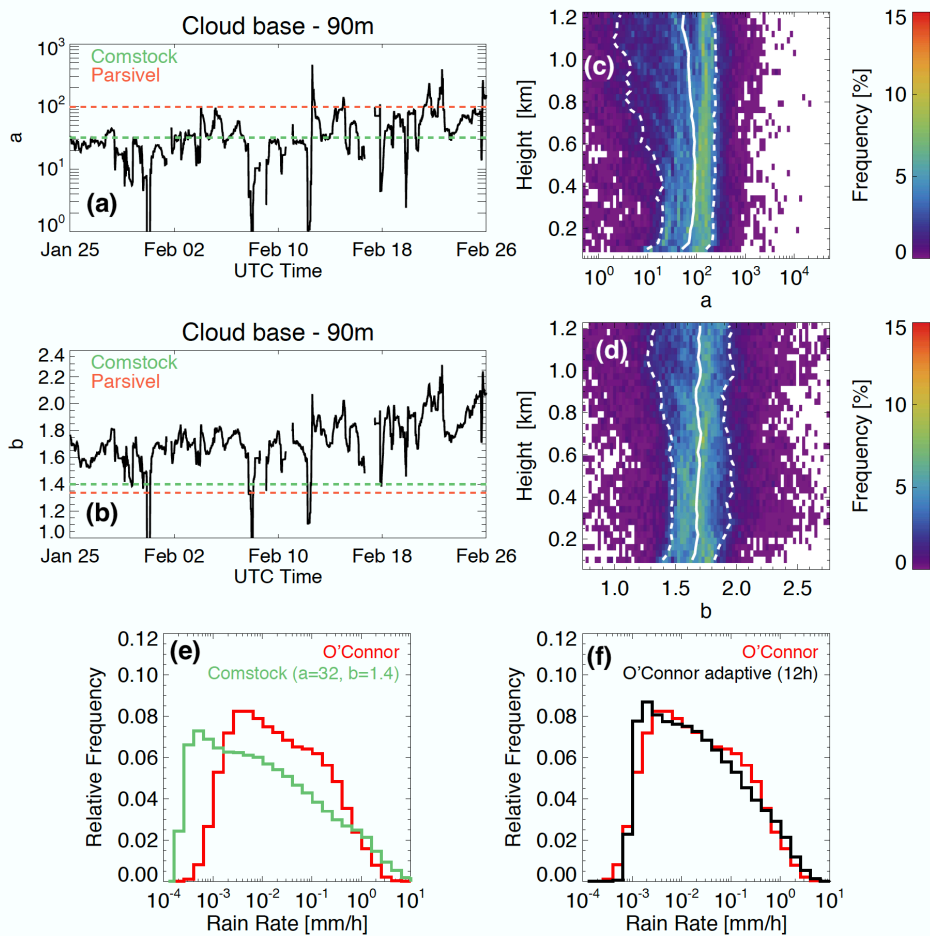
**Figure 6.** Time series of the α (a) and β (b) coefficients used to estimate precipitation rate 90 m below cloud base height for a 30-day long period that overlaps with the second phase of the ACE-ENA field campaign. For the same time period, distribution of the α (c) and β (d) coefficients with height along with their median (solid line) and 25th and 75th percentile values (dashed line). Precipitation rate distributions retrieved using the O'Connor et al. (2005) technique (red) and estimated using the adaptive coefficients (f, black) or the fixed coefficients proposed by *Comstock et al.*, [2004] (e, green). *Comstock et al.*, [2004] coefficients and coefficients determined from disdrometer observations are both presented in panels a and b using dashed green lines and orange lines respectively.
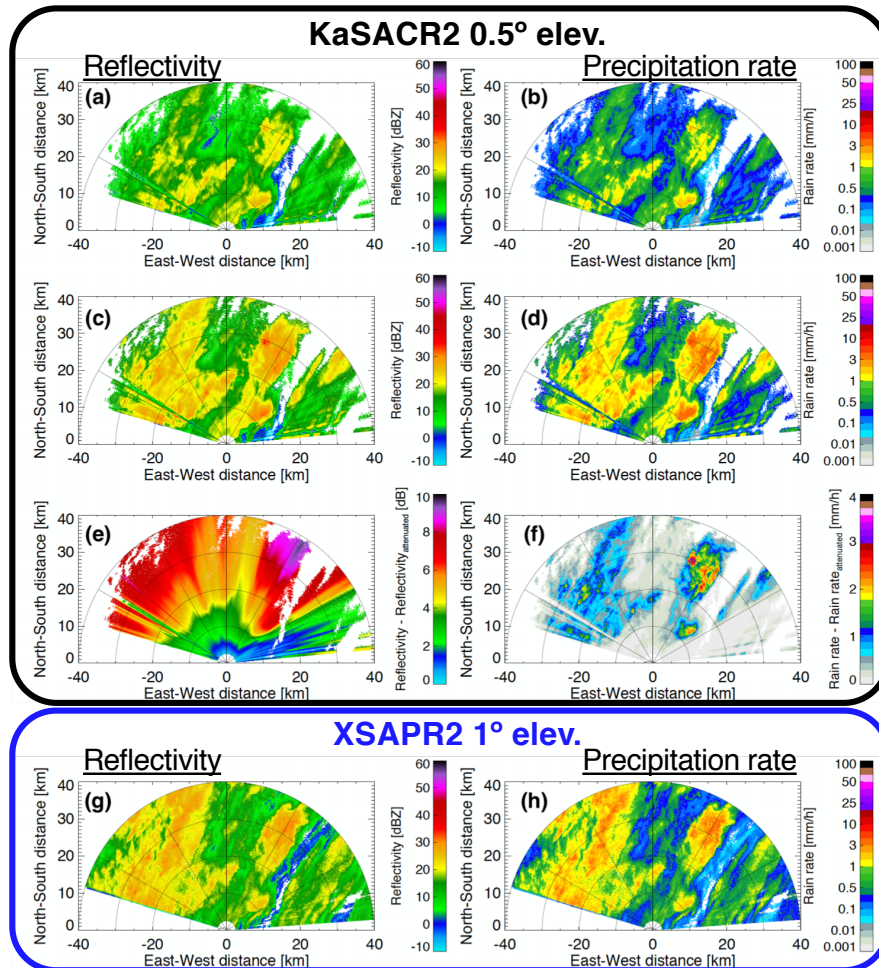
929
Figure 7. Example of observations/retrievals of the conditions happening on 02/13/2018 at
00:10 UTC. Shown for KaSACR2 perfoming 0.5° elevation PPI a) radar reflectivity field
corrected for gaseous attenuation neglecting liquid water attenuation and b) corresponding
precipitation rate retrieved using adaptive Z-R relationships; c) radar reflectivity field
corrected for both gas and liquid water attenuation and d) corresponding precipitation rate; e)
difference between a and c showing the range-accumulated radar reflectivity liquid water
attenuation correction and f) the corresponding precipitation rates bias. The upper panels (g)
and (f) show simultaneously collected XSAPR2 1.0° PPI observations for reference.
938
939

Atmospheric
Measurement
Techniques
Discussions
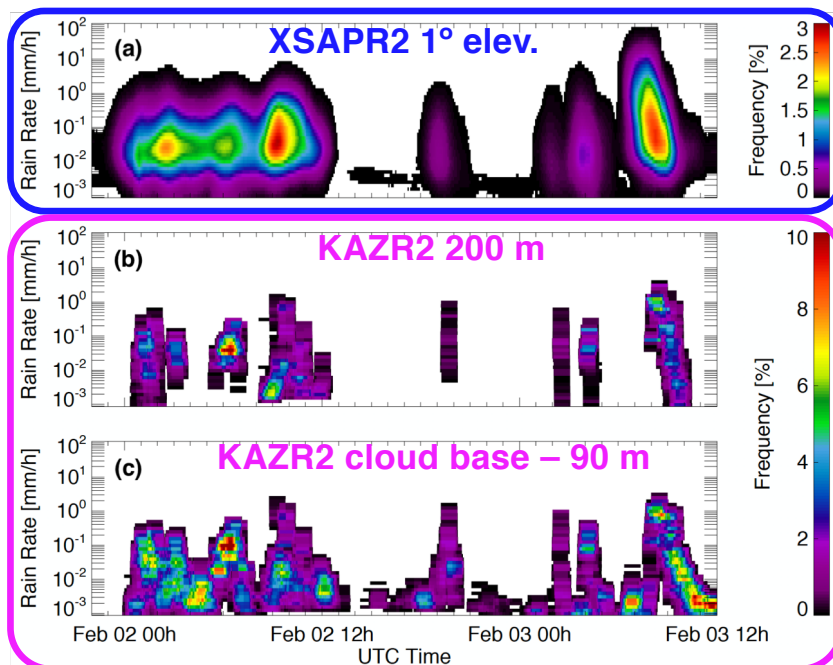
Figure 8. For a 36-h period (00:00 UTC February 2 to 12:00 UTC February 3), hourly probability density functions (pdfs) of precipitation rate estimated from a) XSARP2 when performing a 1 ° elevation PPI scan, b) KAZR2 200 m from the surface and c) KAZR2 90 m below cloud base height
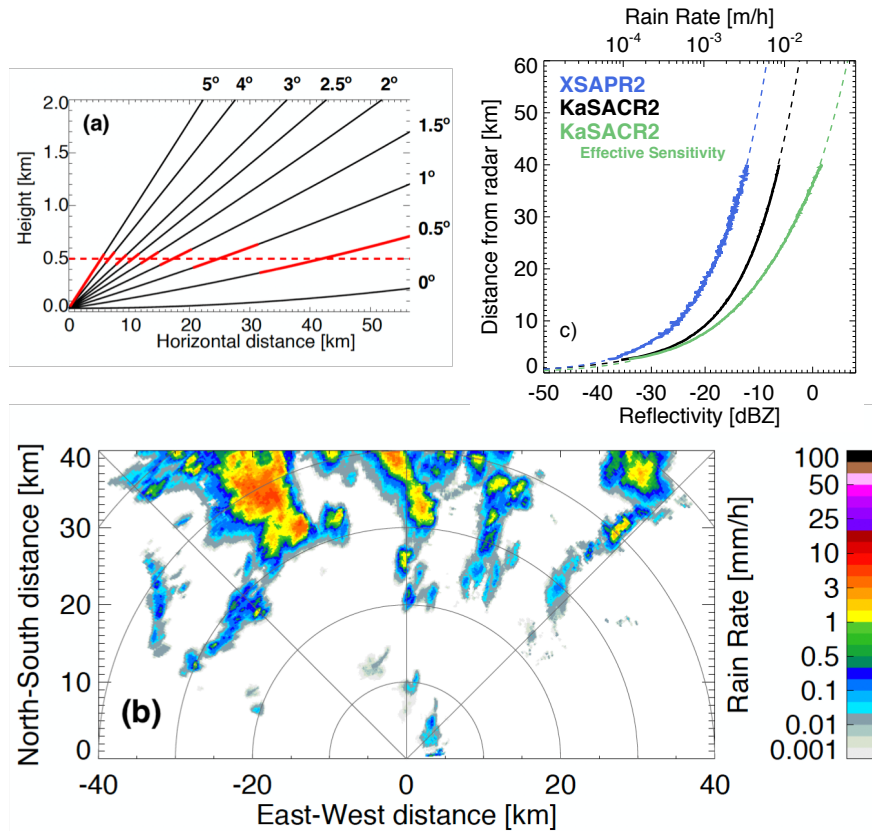
Figure 9. a) PPI scan geometry and b) Cartesian coordinate constant altitude plan position indicator (CAPPI) map of precipitation rate constructed around an altitude of 500 m using XSAPR2 observations collected 21/02/2018 on at 15:00 between 1 and 5° elevation. c) Theoretical sensitivity of the XSAPR2 (blue) and KaSACR2 (black) along with the KaSACR2 "effective" sensitivity considering it is affect by gas attenuation (green).

Atmospheric
Measurement
Techniques
Discussions
Open Access
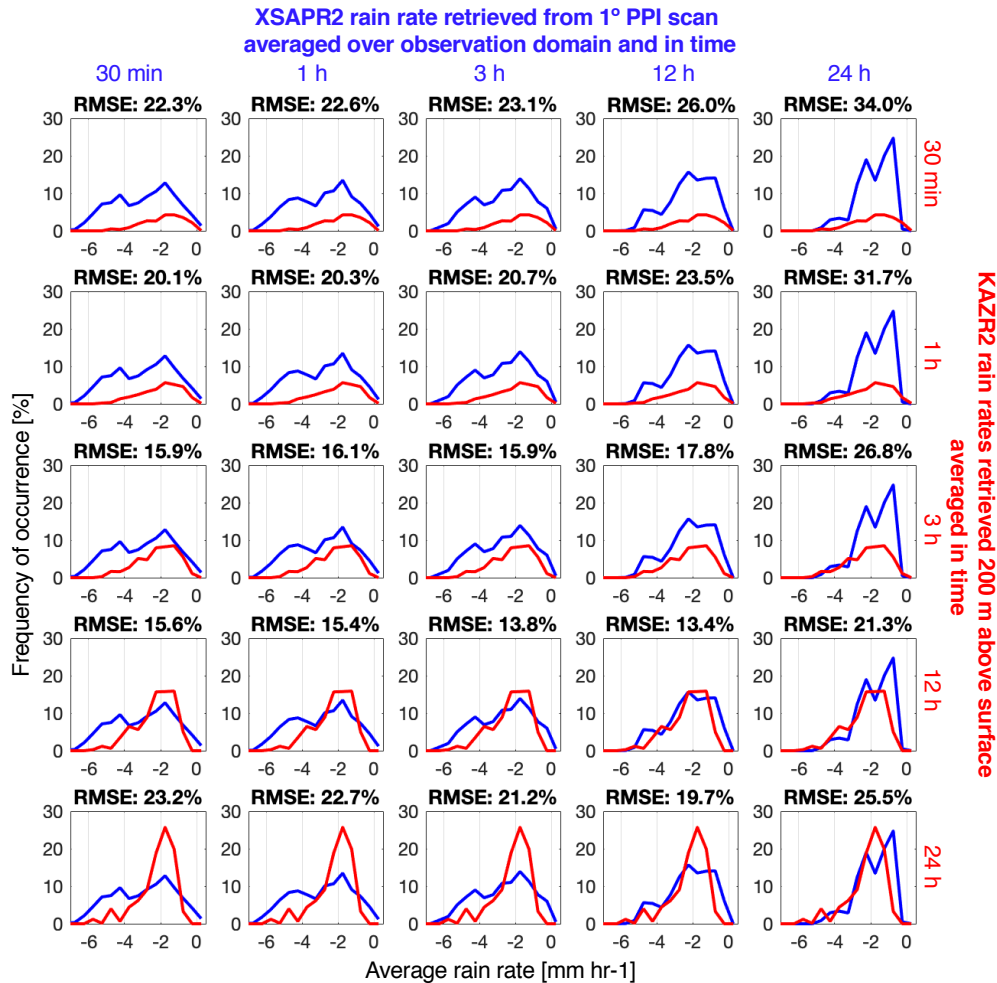
Figure 10. Probability density function of average (over different time windows) precipitation rate as estimated the XSAPR at 1° elevation over the domain between 2.5 and 40 km (blue) and as estimated by the KAZR2 at 200 m (red). Over each box is the root mean square error (RMSE) on the frequency of occurrence of precipitation rate estimated in 0.5 mm hr^{-1} bins between -8 and 0.5 mm hr^{-1}.